

Virtual friction subjected to communication delays in a microgrid of virtual synchronous machines

Original

Virtual friction subjected to communication delays in a microgrid of virtual synchronous machines / Reißner, Florian; Mallemaci, Vincenzo; Mandrile, Fabio; Bojoi, Radu; Weiss, George. - In: IEEE JOURNAL OF EMERGING AND SELECTED TOPICS IN POWER ELECTRONICS. - ISSN 2168-6777. - ELETTRONICO. - (2023).
[10.1109/JESTPE.2023.3276019]

Availability:

This version is available at: 11583/2978540 since: 2023-05-16T13:20:41Z

Publisher:

IEEE

Published

DOI:10.1109/JESTPE.2023.3276019

Terms of use:

This article is made available under terms and conditions as specified in the corresponding bibliographic description in the repository






Publisher copyright

IEEE postprint/Author's Accepted Manuscript

©2023 IEEE. Personal use of this material is permitted. Permission from IEEE must be obtained for all other uses, in any current or future media, including reprinting/republishing this material for advertising or promotional purposes, creating new collecting works, for resale or lists, or reuse of any copyrighted component of this work in other works.

(Article begins on next page)

Virtual friction subjected to communication delays in a microgrid of virtual synchronous machines

Florian Reißner , Vincenzo Mallemaci , *Student Member, IEEE*, Fabio Mandrile , *Member, IEEE*,
Radu Bojoi , *Fellow, IEEE*, George Weiss , *Member, IEEE*

Abstract—*Virtual synchronous machines* (VSMs) have become popular solutions for grid-tied inverters, suited to work on AC-grids with an increasing share of distributed energy sources and storage. However, just like real synchronous machines, VSMs may experience power oscillations. Recently, a new damping concept called *virtual friction* (VF) has been proposed that makes use of real time communication between several inverters. VF introduces an additional damping torque in the swing equation of the VSM, proportional to the deviation of the virtual rotor frequency from the *center of inertia* (COI)-frequency. VF can apply high damping without imposing a strong response in the output power of the VSM during frequency transients. However, VF requires the transmission of frequencies over a communication network, which may suffer from transmission delays. We give an experimental proof of concept of VF both in an isolated microgrid and in grid connected operation of a 45kVA setup consisting of three VSMs realized by three-phase two-level IGBT-based inverters¹. We consider continuous constant and discontinuous varying time delays and show theoretically and experimentally under what conditions delays can impact the output powers of the VSMs. Further, we show how to correctly estimate the COI-frequency with transmission delays using timestamps to align individual signals.

Index Terms—Virtual synchronous machine, virtual friction, microgrid, frequency synchronization, communication delays, latency, damping torque

I. INTRODUCTION

Recently, *virtual synchronous machines* (VSMs) have become a prominent technology for inverter interfaced power sources like renewables and storage [2]–[11]. As power converters, VSMs mimic the behavior of traditional synchronous generators, providing important grid services such as inertial support and frequency droop. However, since they are based on digital algorithms rather than on electro-mechanics, interesting new possibilities arise for controlling the overall system.

One such new control method is called *virtual friction* (VF) [12], [13], which is meant to damp low frequency oscillations in the grid. Traditionally, such oscillations are damped by local feedback such as frequency droop, damper windings

and power system stabilizers [14], [15]. VF uses remote information from other generators and it works like this: Using digital communications, the *center of inertia* (COI)-frequency of the grid, ω_C , a weighted average of the frequencies of all VSMs, is estimated. This enables the application of an additional damping torque to the swing equation of each VSM, proportional to the deviation of the virtual rotor frequency of this VSM from ω_C . One benefit of this is a significantly lower injection of excess power during grid frequency drops, as compared to using an equivalent amount of frequency droop. This is especially advantageous for power plants connected to inverters where limitations of the electronics or of the primary energy source, such as solar or wind, do not allow such a sudden increase in output power. The paper [13] showcased the damping performance of VF in a microgrid of 4 VSMs through simulations and theoretical analysis.

The paper [16] has investigated the influence of VF as opposed to frequency droop on the region of attraction of the preferred stable equilibrium point of the same microgrid that is investigated here. Results suggest that VF can increase this region of attraction and hence it may be a more robust damping strategy than frequency droop alone. We propose to use a combination of frequency droop and VF.

In order to send the individual (virtual) rotor frequencies required for the calculation of the COI-frequency ω_C , and then to send back ω_C , a communication network is required between the different VSMs and a *central controller* (CC). Depending on the infrastructure that is used, such a network inherently introduces delays due to data transmission, propagation and processing [17]. In modern 5G and fiber optical communication, latency can be below 1ms [18]–[20] while for public 4G networks, latency is around 50ms [19], [21]. Roundtrip delays in commercial long distance optical fiber networks have been reported to be around 100ms with little impact of distances up to a few thousands of km [22]. When using modbus, the authors of [23] reported delays below 100ms in a lab setup.

The communication network needed for secondary control in a microgrid depends on the chosen architecture [24]. While the classical approach employs a central secondary controller, also decentralized approaches are possible. It was shown in [24] that such distributed secondary control can be negatively impacted by delays. Instability can occur for large delays (around 600ms). Communication delays between a CC and local inverter controllers have also been investigated in [23] using time-varying delays with a mean of 68ms. Here the CC sent reference signals for power angles and local voltages. The

This research was co-funded by the European Union's Horizon 2020 research and innovation program under the Marie Skłodowska-Curie grant agreement no. 861398 and by the Ministry of Energy, Israel under contract no. 219-11-128. V. Mallemaci, F. Mandrile and R. Bojoi are with the Energy Department "Galileo Ferraris" (DENERG), Politecnico di Torino, 10129 Torino, Italy. F. Reissner and G. Weiss are with the School of Electrical Engineering, Tel Aviv University, Ramat Aviv 69978, Israel. (e-mail: reissner@tauex.tau.ac.il, vincenzo.mallemaci@polito.it, fabio.mandrile@polito.it, radu.bojoi@polito.it, george.weiss@tauex.tau.ac.il)

¹This paper extends our results presented in [1]. Our new contributions in this paper mainly are a detailed theoretical and experimental analysis of delays as well as the demonstration of a modified ω_C calculation in grid connected mode for better damping in such cases.

authors of [24] proposed to use a Smith predictor at the local controller level to compensate for delays. We note here that there exist approaches to estimate the COI-frequency locally at each VSM to achieve damping, so that no communication network is required, see for example [25].

In this paper we investigate the computation of ω_C at a CC and its use for VF. As in our conference paper [1], we compare the system behavior when mainly VF is used to provide damping, with cases where damping was applied using (high) frequency droop only. We extend the results in [1] by a theoretical analysis of delays and their impact on the damping performance of VF. We show that the impact of delays varies greatly with their location and size. In particular, if the delays from the CC to the VSMs are equal, then they have no impact on the power output of the VSMs. We show that the alignment of signals by using timestamps is efficient to keep the damping performance of VF strong when delays are present. Furthermore, we propose an extension of the COI-frequency suitable for mixed grids, where not all the machines can communicate to the CC. Such a scenario is likely if VSMs are integrated into already existing grids. Since VF is a damping torque, it is not suitable for conventional grid-following inverters (e.g. based on *phase locked loops* (PLLs)) which still are much more commonly used than VSMs. On the other hand, the speed control of real synchronous generators is too slow, so that VF cannot be used on these machines either. When using VF in such mixed grids, VF can still be an efficient damping method for VSMs, when using a modified COI-frequency formula. We mention that in our paper [13], we have considered only the case of equal delays, which means that the signals from all the VSMs to the CC are delayed by the same amount.

The remainder of this paper is structured as follows. We give a brief theoretical description of the VSM and the VF mechanism in Sect. II. In Sect. III, we analyze the dynamics of the investigated microgrid and the effects of communication delays. In Sect. IV we present our experimental setup and show results obtained for both an islanded microgrid and one that is connected to the main grid. We propose an extension of the COI-frequency calculation for the latter case. Finally, we show the impact of delays on the system for two delay models, using constant and random time-varying delays.

II. SYSTEM DESCRIPTION

A. Virtual synchronous machines

In Fig. 2 we show the (simplified) electric circuit of phase a of the inverter, phase b and c are identical. The inverter leg of phase a is controlled by the PWM signal generator unit based on the reference voltage g_a . The switches of the inverter generate the output voltage \tilde{g}_a , whose average voltage over one switching cycle is g_a . An LCL filter with inductors L_s , L_2 and capacitor C_s is used to filter out the switching noise in \tilde{g}_a . The resistive parts of the coils are denoted by R_s and R_2 , respectively. Sensors measure the current passing through L_s and the voltage v_a on the filter capacitor.

We briefly introduce here the VSM algorithm used in our experiments in Sect. IV. A full description of this VSM algorithm can be found in [26] (see also [27], [28]). The

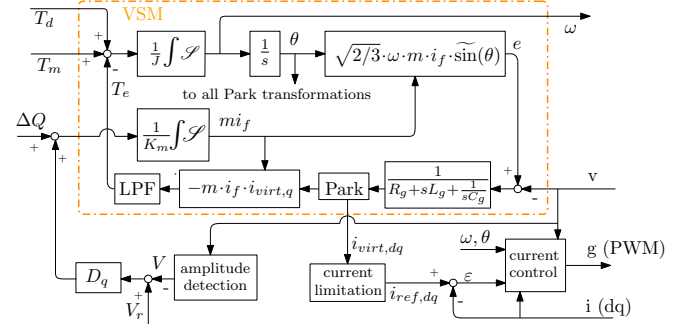


Figure 1: A simplified block diagram of the VSM from [26] showing the swing equation (torque balance), an integral controller for the field current i_f , a virtual impedance block and the fast *output current controller* (OCC). The latter ensures that the output currents i_{dq} track the reference currents $i_{ref,dq}$.

relevant parts of this algorithm, namely the swing equation, the reactive power control and the fast *output current controller* (OCC), as shown in Fig. 1, are described in the following. The torque equation of the VSM in [26] is

$$J\omega = \int \mathcal{S}(T_m - T_e + T_d)dt, \quad (1)$$

where ω and J are the VSMs frequency and inertia respectively, T_e is the electric torque, T_d is the combined damping torque, as shown in Fig. 3 and T_m is the mechanical torque, obtained from the active and reactive power set points. $\int \mathcal{S}$ denotes the saturating integrator from [26], [27], [29]: an integrator that maintains its state and output within a given interval. The rotor angle θ is obtained by integrating the rotor frequency of Eq. (1) (modulo 2π). The rotor angle θ is used for all dq -transformations and for calculating the synchronous internal voltages $e = [e_a \ e_b \ e_c]^\top$. These are

$$e = \sqrt{\frac{2}{3}} m i_f \widetilde{\sin \theta},$$

where i_f is the rotor field current, $m > 0$ is an inductance constant and $\widetilde{\sin \theta} = [\sin \theta \ \sin(\theta - \frac{2\pi}{3}) \ \sin(\theta + \frac{2\pi}{3})]^\top$. The difference between e and the measured grid voltage $v = [v_a \ v_b \ v_c]^\top$ is applied to a series RLC virtual impedance with parameters R_g , L_g and C_g to calculate the virtual currents i_{virt} . After Park-transformation, their q -component $i_{virt,q}$ is employed to determine the electric torque $\tilde{T}_e = -m i_f i_{virt,q}$. Low pass filtering this gives the torque T_e in (1). i_f is regulated by an integral controller, also a saturating integrator:

$$m i_f = \frac{1}{K_m} \int \mathcal{S}(D_q(V_r - V) + \Delta Q)dt,$$

where $\Delta Q = Q_{set} - Q$ is the difference between the reactive power output Q and its setpoint Q_{set} , $D_q > 0$ is the voltage droop coefficient, V is the amplitude of the measured grid voltages, V_r is the reference voltage amplitude and $K_m > 0$ is the inverse controller gain.

Finally, the OCC generates the voltage references g sent to the PWM generator and ensures that the measured output currents track the current references i_{ref} . To prevent overcurrents, the current references i_{ref} are determined by a limitation block. In addition to the tracking error $\varepsilon = i_{ref,dq} - i_{dq}$, the OCC receives also ω , θ , v and i , see [26].

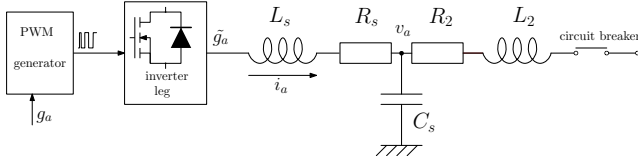


Figure 2: Phase a of the simplified power circuit of the inverter.

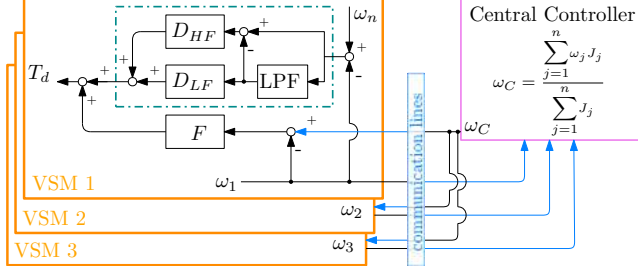


Figure 3: In a VSM with VF, the damping torque T_d is obtained by adding the torques of VF, HF- and LF-droop. While the frequency droop torque is proportional to $\omega - \omega_n$, the VF damping torque is proportional to $\omega - \omega_C$ (See (4) for ω_C). The signals ω_C , ω_1 , ω_2 and ω_3 are sent over a communication line which introduces delays. Delayed signals are colored in blue.

Fig. 3 shows how the damping torque T_d for the VSMs in this work is calculated. It consists of VF, *low frequency* (LF)-droop and *high frequency* (HF)-droop, where the HF-droop signal is obtained by subtracting the output of a first order low pass filter from the unfiltered signal. In our realization, the time constant of this filter is 1s, and the HF-droop coefficient D_{HF} is 1-6 times larger than the LF-droop coefficient D_{LF} . The VF torque is $F \cdot (\omega - \omega_C)$, where ω_C (the weighted average of the generator frequencies) is calculated by a CC, see (4) and F is the VF coefficient. Note that the differences $(\omega - \omega_C)$ only depend on the differences of the VSM frequencies. These differences can be kept small by sufficiently increasing the VF coefficient F , such that even during a large frequency drop, $(\omega - \omega_C)$ remains small compared to $(\omega - \omega_n)$ [13]. As a consequence, the active power output during such events remains within reasonable bounds, even for large F .

It is helpful, for the theoretical analysis, to separate the system dynamics into two timescales: a fast one that models the dynamics of the OCC and the switches of the VSM ($< 1\text{ms}$) and a slow one, which models the dynamics of ω , θ and i_f ($> 10\text{ms}$). An even slower timescale ($> 50\text{s}$) could be used, if secondary control is considered relevant, however this shall be ignored here. We assume that the OCC is properly tuned and the impedance of the grid is not too high, such that the OCC is stable and ensures that the current tracking error $\varepsilon \approx 0$. Hence, on the slow timescale, which is the one of interest for us here, the dynamics of the OCC can be neglected. Under these assumptions, the VSM can be described by a simplified model, described in the following section.

B. Modeling a grid comprising several VSMs

For the theoretical discussion of the power oscillations in a microgrid comprising three VSMs, we briefly introduce a simplified, but powerful model that is known to represent this type of dynamics well: the *friction enhanced power system* (FEPS) model [13]. This model is obtained from the *network reduced power system* (NRPS) model (see [30], [31] and Chapter 6 in

[32]) by including VF. As the stability analysis of these models has been presented in the mentioned publications, we refrain from a detailed analysis. The FEPS model represents a power grid with N VSMs, connected via a passive network modeled by constant (complex) impedances. Each VSM is modeled as a constant amplitude, variable frequency, balanced three-phase voltage source, generating positive sequence only. Under these assumptions, the FEPS model is given by the following N equations. The swing equation for each VSM is:

$$M_j \ddot{\theta}_j + \omega_n (F_j + D_j) \dot{\theta}_j = P_{set,j} + \omega_n (D_j \omega_n + F_j \omega_C) - P_{e,j}, \quad (2)$$

where D_j is the frequency droop coefficient, F_j is its VF coefficient and $P_{set,j} = T_m \omega_n$ is the set power of VSM j . Clearly, (2) is obtained from (1) by differentiating, neglecting saturation effects, multiplying with ω_n and introducing $M_j = \omega_n J_j$, where J_j is the inertia of VSM j , as well as $P_{e,j} = \omega_n T_e$. In this model we have assumed that the HF and LF droop coefficients of generator j are equal, namely D_j . We note that the NRPS model is written as a power balance equation, whereas the VSM equation (1) is a torque balance equation. In order to avoid confusion in the following, we defer here from the standard notation of the NRPS model and continue to use the droop constant D_j expressed in $\text{kg} \cdot \text{m}^2/\text{s}$ as in Fig. 3. This leads to an additional multiplication by the (constant) ω_n in (2) in front of F_j and D_j .

The electric power $P_{e,j}$ depends on the differences between the rotor angles θ_k of the VSMs:

$$P_{e,j} = \sum_{k=1}^N a_{jk} \sin(\theta_j - \theta_k - \varphi_{jk}), \quad (3)$$

where $a_{jk} = |Y_{jk}| E_j E_k$ for $1 \leq j, k \leq N$, with $[Y_{jk}]$ being the admittance matrix of the grid including the loads, E_j is the amplitude of the output voltage of VSM j and $\varphi_{jk} = \arg Y_{jk} - \frac{\pi}{2}$. (Note that we have deviated from the notation in [30] where the authors require $a_{jj} = 0$. This is however only a choice of notation.) The center of inertia frequency ω_C is defined as in [33]: denoting $\omega_k = \dot{\theta}_k$,

$$\omega_C = \frac{\sum_{k=1}^N M_k \omega_k}{\sum_{k=1}^N M_k}. \quad (4)$$

We introduce the following notation for the damping ratio ρ_j and the share of VF of the overall damping σ_j :

$$\rho_j = \frac{D_j + F_j}{J_j}, \quad \sigma_j = \frac{F_j}{D_j + F_j}, \quad 1 \leq j \leq N.$$

The value of $D_{HF,j}$ is used instead of D_j to define ρ , if $D_{HF,j} \neq D_{LF,j}$, since HF-droop mainly defines the system damping. The parameters J_j , D_j and F_j can be used to tune system behavior for a given grid. The correlation of these parameters with the damping and the frequency of power oscillations will be described with the help of a linearized version of the FEPS model.

It is useful to define the *grounded rotor angles*

$$\delta_j = \theta_j - \theta_n. \quad (5)$$

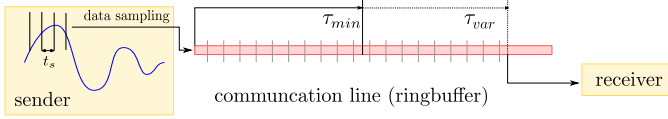


Figure 4: Delay **model 2**: with a frequency f_s , samples are fed into a buffer by the sender. At each sampling moment t_s , the receiver reads (and removes) every sample from the buffer delayed by at least $\tau(t) = \tau_{min} + \tau_{var}$. It may be that no such samples are in the buffer, then no new information is received at t_s . If new info has been received, then τ_{var} gets assigned a new random value.

We are interested in *uniform grids* where the ratios of frequency droop to inertia D_j/J_j and virtual friction to inertia F_j/J_j are the same for all VSMs. In such grids we define:

$$d = \frac{D_j}{J_j}, \quad f = \frac{F_j}{J_j}. \quad (6)$$

C. Modeling of delays

We employ two different models for delays: **Model 1** assumes constant delays (between 0s and 5s) and a sampling period equal to the switching period of the inverters, such that sampling effects are negligible. The simplicity of this model helps to isolate the effects of delays on the behavior of the grid, and it will be used for recognizing the most important delay effects. **Model 2** assumes a variable network delay and a sampling frequency f_s which is lower than the switching frequency. In this model, the transmission delay has a minimum value of τ_{min} and an additional randomly varying delay of τ_{var} . τ_{var} is uniformly distributed between 0 and $\tau_{var,max}$. We illustrate **model 2** in Fig. 4. This delay model is difficult to analyze theoretically, but can be used to demonstrate the impact of more realistic network delays.

III. THEORETICAL ANALYSIS

A. Stability of the linearized FEPS model

We have linearized the FEPS model around the steady state of the uniform and islanded microgrid shown in Fig. 9 when using the line impedances, loads and set powers as defined in Sect. IV-A1 and when L_2 is disconnected. We show here the influence of J , D , ρ and σ on the dynamics of the system. In the following, J and D refer to the base values of inertia and frequency droop. The respective values for VSM j are obtained by $J_j = x_{b,j}J$ and $D_j = x_{b,j}D$ with $x_b = [0.6 \ 0.4 \ 0.3]$. The FEPS model of this grid has 5 poles, of which two pole pairs correspond to the dynamics of δ_j from (5) (which are closely linked to the output powers of the VSMs). They may be complex valued for some values of J and D . The fifth pole corresponds to the frequency dynamics of the system and is always on the real axis.

Fig. 5 shows the 5 poles for $J = 0.5 \text{ kg} \cdot \text{m}^2$, $\rho = 40 \text{ s}^{-1}$ and $\sigma = 1$ as large red marks. In this limit case only VF and no frequency droop is used, such that one pole is at the origin. Two other poles are on the real axis and two are complex conjugate. For this pole pair, we show isolines of constant J , D and ρ . They indicate how these parameters impact the position of the pole pair, if the poles are complex conjugate (in case they become real, the isolines do not give

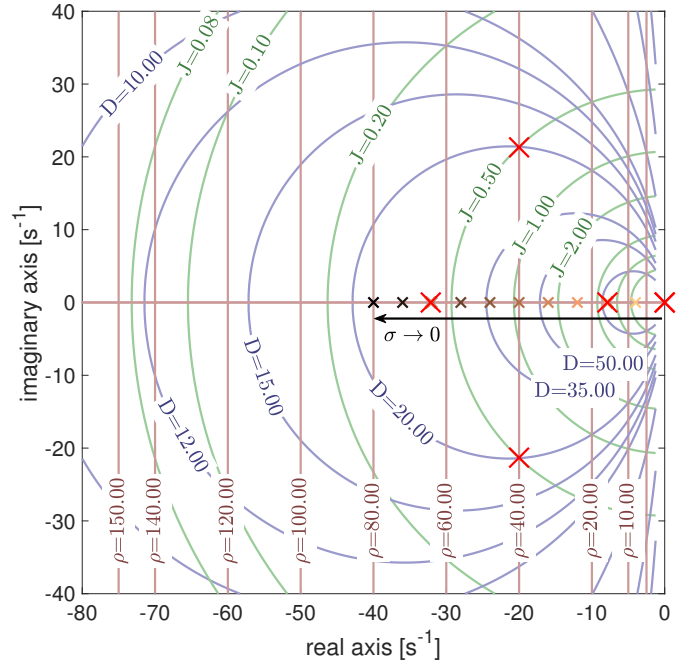


Figure 5: Poles of the linearized FEPS model representing the network from Fig. 9 with data as in Sect. III-A. There are 5 poles for the 3 VSMs system of which 4 correspond to the angular oscillations and one to the COI-frequency dynamics. The large red marks indicate the poles for $\sigma = 1$, where the pole at the origin is related to the frequency dynamics. When decreasing σ from 1 to 0, this pole moves towards the left to $[-40 \ 0]$, the other poles remain unchanged. Lines of constant J , D and ρ are marked in light green, blue and red respectively. They indicate how these parameters impact the position of the complex pole pair. The values of D and J noted on these isolines must be multiplied by $[0.6 \ 0.4 \ 0.3]$ to obtain the respective value for VSM 1, 2 and 3.

any information anymore). Note here that for the second pole pair, it is possible to draw similar isolines for J and D . They have been excluded here for readability. For decreasing σ from 1 to 0, the frequency related pole moves from the origin towards the point $[-40 \ 0] \text{ s}^{-1}$ (marks from bright to dark) while the remaining 4 poles do not move. σ correlates inversely with the coupling strength of the VSM frequency to ω_n . Fig. 6 illustrates this behavior, here the frequency of VSM 3 is plotted subsequent to a load disconnection. In the extreme case, if $\sigma = 1$ (light orange), the system frequency increases infinitely, with the pole at the origin acting as an integrator. The power imbalance between the sum of the set powers and the consumed electrical power in the grid defines the slope of this frequency increase. A higher σ (with the same damping) leads to a lower coupling of the output power of the VSM with a frequency change. Of course, in order to set a reference frequency ω_n and to not move the σ -dependent pole to the origin, some level of frequency droop is required.

B. Dynamics of the COI-frequency

In the following, we investigate the dynamics of ω_C , showing that little or no oscillations are expected in this variable if the received signals are aligned or the delays are small.

For a weighted mean like ω_C from (4), it is known that

$$\min \{\omega_k\} \leq \omega_C \leq \max \{\omega_k\}. \quad (7)$$

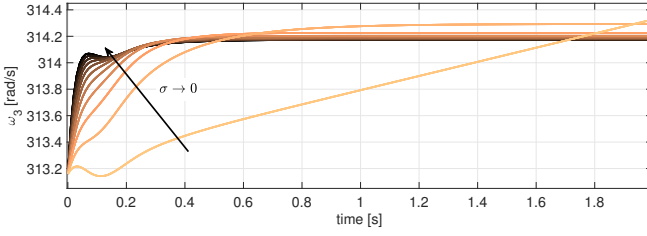


Figure 6: FEPS model: plots of ω_3 after disconnecting a load starting from steady state at the initial frequency $\omega_3 = 313.15 \text{ rad/s}$. We show curves for increasingly high σ from 0 (light orange) to 1 (black) with fixed damping ratio $\rho = 40 \text{ s}^{-1}$. When no frequency droop is used (i.e. $\sigma = 1$), and if a power imbalance between load and mechanical power input exists, then the model acts as an integrator such that $\omega \rightarrow \infty$ for $t \rightarrow \infty$ (this is the light orange curve).

If the grid is uniform, as in (6), it can be shown that the dynamics of ω_C depend only on the total power balance in the grid. This dependence can be expressed by a first order transfer function. We introduce the following notation:

$$\begin{aligned} M_T &= \sum_{j=1}^N M_j, & P_M &= \sum_{j=1}^N P_{set,j}, \\ P_D &= \omega_n \sum_{j=1}^N D_j, & P_L &= \sum_{j=1}^N a_{jj} \sin \varphi_{jj}, \\ \Delta_{jk} &= \theta_j - \theta_k. \end{aligned} \quad (8)$$

Let E be the set of edges in the network graph, $E = \{(j, k) | 1 \leq j < k \leq N\}$. In a fully connected graph, there are $n_e = \binom{N}{2} = \frac{N!}{2(N-2)!}$ such edges. Note that the FEPS model of a real, connected network is obtained by Krohn reduction and therefore is expected to be fully connected. By differentiating (4), and using (2) and (8):

$$\begin{aligned} M_T \dot{\omega}_C &= \sum_{j=1}^N M_j \dot{\omega}_j \\ &= P_M + P_D + M_T f \omega_C + P_L - (d + f) \sum_{j=1}^N (M_j \omega_j) \\ &\quad - \sum_{j=1}^N \sum_{k=1}^N a_{jk} \sin(\theta_j - \theta_k - \varphi_{jk}) \end{aligned} \quad (9)$$

Substituting ω_C on the right side of the equation gives:

$$\begin{aligned} M_T \dot{\omega}_C &= P_M + P_D + M_T f \omega_C + P_L - (d + f) M_T \omega_C \\ &\quad - \sum_{e \in E} a_e [\sin(\Delta_e - \varphi_e) + \sin(-\Delta_e - \varphi_e)] \end{aligned}$$

Using a trigonometric identity, this becomes:

$$M_T (\dot{\omega}_C + d \omega_C) = u(t), \quad (10)$$

where

$$u(t) = P_M + P_D + P_L - \sum_{e \in E} 2a_e \cos(\Delta_e) \sin(\varphi_e). \quad (11)$$

We note that (10) is the equation of a first order low pass filter from u to ω_C . Here u is the power balance of the grid with the total mechanical power input P_M , a constant P_D added by frequency droop, and the constant P_L , which can

be interpreted as the local short circuit power consumption. In (11), $P_L - \sum(\dots)$ is the total electrical power consumption in the network, while the terms P_M , P_D and P_L are constants. The sum $\sum(\dots)$ depends on the rotor angle differences of the VSMs in the network. For a network with purely inductive lines between all generators and with loads connected only directly to the generators (an unlikely scenario) we have $\varphi_e = 0 \forall e \in E$. In such a case u in (10) becomes a constant:

$$u = P_M + P_D + P_L,$$

and hence ω_C converges to a steady state value. Of course, in a real grid, lines are not only inductive, and the loads are distributed in the network, instead of being connected directly to the generators. Then u depends on $\cos(\Delta_e)$. Thus, small variations in Δ_e around zero have little impact on ω_C .

The equation (10) shows that the dynamics of ω_C correspond to a single pole on the real axis: for increasing $\sigma = \frac{f}{d+f}$ - or equivalently, for decreasing d - this pole moves to the right, as can be seen also in Fig. 5.

C. Delays

We assume here that the COI-frequency is calculated by a CC (which may also execute additional tasks such as optimal dispatch or secondary control). Communication delays thus arise for both the signals sent from the VSMs to the CC and for the transmission of ω_C back to the inverters.

Interestingly, in an isolated and uniform microgrid as in (6), the power output of the VSMs is neither impacted by delays from the VSMs to the central processor nor by equal delays from the central processor back to the VSMs (by equal, we mean that the signal ω_C arrives at each VSM after the same amount of time): Indeed, subtracting (2) for VSM j from (2) for VSM N , we get, using the notation from (5):

$$\ddot{\delta}_j + (d + f) \dot{\delta}_j = \frac{P_{set,j}}{M_j} - \frac{P_{set,N}}{M_N} - \frac{P_{e,j}}{M_j} + \frac{P_{e,N}}{M_N}. \quad (12)$$

Note that the terms $f \omega_C$ and $d \omega_n$ have canceled on the right side of the equation. There are $N-1$ such equations describing the dynamics of the grounded rotor angles. Note that the dependence of δ_j on ω_C and ω_n has vanished in (12), so that ω_C does not impact the dynamics of the grounded rotor angles. Indeed, the terms $P_{e,j}$ and $P_{e,N}$, given in (3), can be rewritten using only δ_j (see also [13]). While this result does not state anything about the dynamics of ω_C in such a case, this shows that if all VSMs receive the same (delayed) signal ω_C , the output powers $P_{e,j}$ of the VSMs are not impacted by these delays. We refer to Sect. IV-B1 and IV-B2 for a demonstration of these effects.

It is possible to write a modified version of (9) for a system impacted by delays, if all VSMs receive the same signal $\tilde{\omega}_C(t) = \omega_C(t - \tau)$, with $\tau > 0$. In such a case, $\tilde{\omega}_C$ replaces ω_C on the right side of (9). Using trigonometric identities, as after (10), we can write:

$$\begin{aligned} \dot{\omega}_C + (d + f) \omega_C - f \tilde{\omega}_C &= \\ \frac{1}{M_T} \left(P_M + P_D + P_L - \sum_{e \in E} 2a_e \cos(\Delta_e) \sin(\varphi_e) \right). \end{aligned} \quad (13)$$

Denote the right-hand side of (13) by v . Note that v is a bounded signal. Taking the Laplace transform of (13) we get:

$$\hat{\omega}_C(s) = H(s)\hat{v}(s), \quad H(s) = \frac{1}{s + d + f(1 - e^{-\tau s})}. \quad (14)$$

We note that $\text{Re}(1 - e^{-\tau s}) > 0$ for all $s \in \mathbb{C}_+$ (the open right half-plane), whence $\text{Re}[s + d + f(1 - e^{-\tau s})] > d$ for all $s \in \mathbb{C}_+$. This easily implies that the factor $H(s)$ appearing in (14) is bounded on \mathbb{C}_+ , $|H(s)| < \frac{1}{d}$ for all $s \in \mathbb{C}_+$. In other words, H is a stable transfer function. We remark that in addition H is positive-real and its impulse response is in $L^2[0, \infty)$. The poles of H (there are infinitely many) can be computed using the Lambert W function, see Appendix A in [34]. From the stability of H we conclude that if the system (12) is stable, i.e., its state variables δ_j converge to an equilibrium, then also ω_C converges to an equilibrium value.

At low frequencies $H(s)$ can be approximated by a Taylor expansion of the term $e^{-\tau s}$. Neglecting all terms of higher order, the first order approximation of H is:

$$H(s) \approx \frac{1}{d(Ts + 1)}, \quad T = \frac{1 + \tau f}{d}.$$

This expression for the time constant T of this low pass filter indicates that increasing f and τ slows down the convergence of ω_C , an observation that is confirmed in Fig. 16.

D. Unequal delays and their compensation

While different delay compensation mechanisms have been proposed in the literature (for example the Smith predictor [23], [24], [35]), we show here that aligning the received signals according to a timestamp already proves very effective in maintaining strong damping in spite of delays.

If the received samples are not aligned before summation, the estimate of ω_C (denoted by $\tilde{\omega}_C$) may show strong oscillations during transients, while the real ω_C oscillates very little. In such a case, if delays affecting the signals sent from the CC to the VSMs are also unequal, the damping effect of VF can be significantly degraded, see Fig. 7. The simulation shown in Fig. 7 involves two VSMs connected over a tieline. VSM 1 submits ω_1 and receives ω_C with 80ms delay. The communication delays between the CC and VSM 2 are negligible. The round trip delay of 160ms between the CC and VSM 1 is very close to the period of the inter-area oscillations (which depends on the J_j and $D_j + F_j$, see Sect. III-A). Subsequent to a disturbance (i.e., after a grid reconfiguration, fault or load change), oscillations occurring between the VSMs are observed in ω_1 , ω_2 and $\tilde{\omega}_C$. Without any delay compensation (top) the damping effect of VF is very low and $\tilde{\omega}_C$ strongly oscillates. If for the same system, the frequency of the second generator ω_2 is artificially delayed by 80ms at the CC and therefore aligned with ω_1 , the oscillations in $\tilde{\omega}_C$ vanish and the damping effect is stronger (bottom).

To achieve alignment, signals can be sent with a timestamp that can be obtained, for example, from a GPS module with a typical accuracy below 20ns [23], [36]. Based on this timestamp, the CC can artificially delay all signals to the largest delay τ_{max} such that the $\tilde{\omega}_C$ becomes:

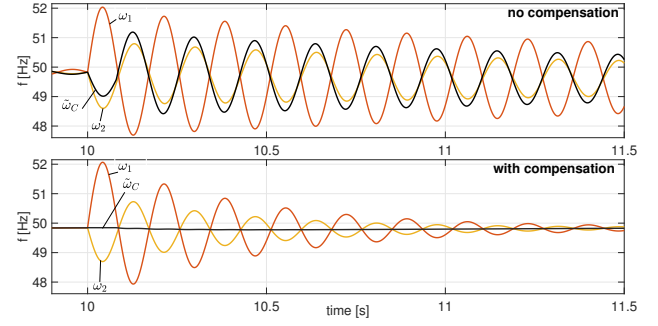


Figure 7: The effect of misaligned signals: the red and yellow lines show the frequencies of two VSMs in an isolated microgrid subsequent to a disturbance at $t = 10$ s with VF. The communication between VSM 1 and the CC is delayed both ways by 80ms (using delay **model 1**). The delay between the CC and VSM 2 is negligible. Top: if signals are not aligned at the CC, $\tilde{\omega}_C$ oscillates (black line), leading to a decreased damping. Bottom: aligning ω_2 with ω_1 , $\tilde{\omega}_C$ remains almost constant and the oscillations decay faster.

$$\tilde{\omega}_C(t) = \frac{\sum_{k=1}^N J_k \omega_k(t - \tau_{max})}{\sum_{k=1}^N J_k}. \quad (15)$$

For the simple case of two VSMs connected via a tieline, we show how to estimate the oscillation frequency and the damping factor. For simplicity, we assume that the VSMs have equal inertia M , set power P_{set} , frequency droop D and VF-constant F . As before, we assume that there are no delays in the communication between VSM 1 and the CC, while between VSM 2 and the CC there is a delay of τ both ways. The FEPS-model of this system is:

$$\begin{aligned} \ddot{\theta}_1 + (f + d)\dot{\theta}_1 &= \tilde{p} + f\tilde{\omega}_C - \frac{a}{M} \sin(\theta_1 - \theta_2 - \varphi), \\ \ddot{\theta}_2 + (f + d)\dot{\theta}_2 &= \tilde{p} + f\tilde{\omega}_C(t - \tau) - \frac{a}{M} \sin(\theta_2 - \theta_1 - \varphi), \\ \tilde{\omega}_C &= \frac{1}{2}(\omega_1 + \omega_2(t - \tau)), \end{aligned} \quad (16)$$

where $\tilde{p} = \frac{1}{M}(P_{set} + \omega_n^2 D - a_0 \sin(\varphi_0))$ and a_0 and φ_0 are the diagonal values of the network admittance matrix and the phase angle matrix. Using the grounded rotor angle $\delta = \theta_1 - \theta_2$, the three equations (16) become:

$$\ddot{\delta} + \tilde{d}\dot{\delta} + c \sin \delta = \frac{f}{2}(\omega_1 + \omega_2(t - \tau) - \omega_1(t - \tau) - \omega_2(t - 2\tau)),$$

where $c = \frac{2a}{M} \cos(\varphi)$ and $\tilde{d} = (d + f)$. We are interested in the effect of τ on the damping and frequency of oscillations in this microgrid. We may look at very small angular disturbances only, so that $\sin(\delta) \approx \delta$. We obtain:

$$\ddot{\delta} + \tilde{d}\dot{\delta} + c\delta = \frac{f}{2}(\omega_1 + \omega_2(t - \tau) - \omega_1(t - \tau) - \omega_2(t - 2\tau)). \quad (17)$$

Because of the symmetry of the system, it appears reasonable to assume that after sufficient time, the two VSMs oscillate with the same frequency and a phase shift of 180° . A solution for (17) can thus be attempted by using the Ansatz:

$$\begin{aligned} \omega_1(t) &= \omega_0 + e^{kt}(k \sin(\nu t) + \nu \cos(\nu t)), \\ \omega_2(t) &= \omega_0 - e^{kt}(k \sin(\nu t) + \nu \cos(\nu t)), \end{aligned} \quad (18)$$

where $k < 0$ and $\omega_0 > 0$ is the equilibrium frequency. This allows us to write δ and its derivatives as:

$$\begin{aligned}\delta(t) &= 2e^{kt} \sin(\nu t), \\ \dot{\delta}(t) &= 2e^{kt} (k \sin(\nu t) + \nu \cos(\nu t)), \\ \ddot{\delta}(t) &= 2e^{kt} ((k^2 - \nu^2) \sin(\nu t) + 2k\nu \cos(\nu t)).\end{aligned}\quad (19)$$

The delayed signal $\omega_1(t - \tau)$ then can be expressed as:

$$\begin{aligned}\omega_1(t - \tau) &= \omega_0 + e^{k\tau} e^{kt} (k \cos(\nu\tau) + \nu \sin(\nu\tau)) \sin(\nu t) \\ &\quad + e^{k\tau} e^{kt} (\nu \cos(\nu\tau) - k \sin(\nu\tau)) \cos(\nu t).\end{aligned}\quad (20)$$

Similar expressions are obtained for $\omega_2(t - \tau)$ and for $\omega_2(t - 2\tau)$. Substituting (18), (19) and (20) in (17) and by comparing the terms multiplied by $\sin(\nu t)$ and $\cos(\nu t)$, we obtain the following equations for k and ν :

$$\begin{aligned}0 &= (k^2 - \nu^2) + \tilde{d}k + c + \frac{f}{2} e^{-k\tau} [\nu \sin(\nu\tau) + k \cos(\nu\tau)] \\ &\quad - \frac{f}{4} [k + e^{-2k\tau} (\nu \sin(2\nu\tau) + k \cos(2\nu\tau))], \\ 0 &= 2k\nu + (d + f)\nu + \frac{f}{2} e^{-k\tau} [\nu \cos(\nu\tau) - k \sin(\nu\tau)] \\ &\quad - \frac{f}{4} [k + e^{-2k\tau} (\nu \cos(2\nu\tau) - k \sin(2\nu\tau))].\end{aligned}\quad (21)$$

Using a numerical solver, τ -dependent solutions can be obtained for (21). Fig. 8 shows these k and ν computed for an example where $M = \omega_n$, $f = 2$, $d = 1$, $a = 65,600$, $\varphi = 0.566$ and $\tau \in [0 \ 0.4]$ (we have taken $J = 1$). Fig. 8a shows a set of such solutions ν (in Hz), indexed from 1 to 9. The dashed horizontal line marks the natural oscillation frequency without delays, $\nu_0 = \sqrt{\frac{\tilde{d}^2}{4} - \frac{2a}{M} \cos \varphi}$ and the vertical dashed lines show the delays τ_0 that match the half period of this ν_0 . The damping for each of these solutions is shown in Fig. 8b. The black solid lines overlapping the red solution number 1 indicate the damping k and frequency ν obtained by simulating the FEPS-model. (For each delay τ , the values are estimated by curve fitting a decaying sine to the signal $\omega_1 - \omega_C$.)

Fig. 8 shows that there are many solutions for k and ν for each τ . Most of these solutions are strongly damped and have an inverse dependency on τ . Solution 1 (with the lowest damping) is predominant until $\tau \approx 0.4$. The damping k of this solution is worst for $\tau = \tau_0$ and has another peak at $\tau = 2\tau_0$. Interestingly, ν of solution 1 shows a negative slope around τ_0 and $2\tau_0$ and $\nu = \nu_0$ at τ_0 and at $2\tau_0$. Solution 3 becomes the predominant (i.e., the least damped) solution for $\tau > 0.4$ so that the black curve (obtained by simulation of the FEPS-model and curve fitting) jumps from solution 1 to solution 3 at $\tau \approx 0.4$. In Sect. IV-B2 we will show that experiments in the 3-VSM microgrid produce similar results.

IV. EXPERIMENTAL VALIDATION

We show experimental results for a microgrid consisting of three VSMs, line impedances, a transformer and loads. The setup is shown in Figs. 9 and 10. S_2 allows to connect the microgrid to an infinite bus or to a load L_1 , both emulated by a programmable AC power supply. There are two voltage levels in the grid, separated through a delta-wye transformer: VSMs G_2 and G_3 are connected on the high voltage side ($190V_{\text{rms}}$)

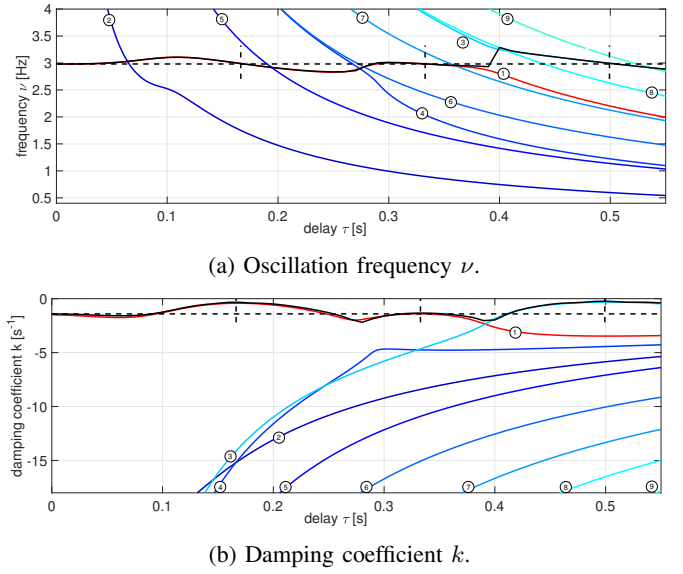


Figure 8: Solutions of (17) for the symmetric 2 VSM microgrid. The black continued line shows the predominant oscillation frequency obtained by simulating the FEPS-model. The horizontal dashed line marks ν_0 and the vertical dashed lines indicate τ_0 , $2\tau_0$ and $3\tau_0$.

and a third VSM (G_1) is connected at the low voltage side ($110V_{\text{rms}}$). L_1 is a 6kW, 1.8kVAr load which is connected in all experiments with an islanded microgrid. The load L_2 consists of three line-to-line connected resistors of 110Ω each, representing a 2.95kW load at $190V_{\text{rms}}$. The line impedances (per line) are $Z_1 = 2\text{mH}$, $Z_2 = 4\Omega$, 5mH , $Z_3 = 0.3\text{mH}$. All inverters have a three phase, two-level, IGBT based topology using a switching frequency of 10kHz. G_2 and G_3 use an LCL filter with values $L_s = 2\text{mH}$, $C_s = 5\mu\text{F}$, $L_2 = 3.3\text{mH}$. The values of the LCL filter of G_1 are $L_s = 545\mu\text{H}$, $C_s = 22\mu\text{F}$, $L_2 = 120\mu\text{H}$. G_1 is powered by a 300V DC power supply and employs an internal step-up converter to raise the DC voltage to 380V. G_2 and G_3 are connected to the same DC power supply at 650V. All inverters employ space vector modulation and have a power rating of 15kW. G_1 is controlled by a dSpace DS1005 board (DS1), while G_2 and G_3 are controlled by a dSpace MicroLabBox (DS2). Delay models were implemented on DS2 and a CAN-bus is used to communicate ω_C and ω_1 between the two systems. In addition, a synchronization signal is sent from DS2 to DS1 in order to allow alignment of the recorded data for postprocessing and plotting.

This section first focuses on experimental results without delays, similar to what was presented in [1]. Both islanded operation and grid connected operation are shown. For the latter we demonstrate the mentioned modified COI-frequency, which takes into account the frequency of the main grid to improve damping in such cases. Subsequently, we focus on experiments with delays. We show results with the islanded microgrid, illustrating our theoretical findings of Sect. III-C as well as delays in grid connected mode. Finally we show results using delay **model 2**.

A. Fast communication (no delays)

We compare the damping of oscillations subsequent to a disturbance created by connecting L_2 in the islanded case to

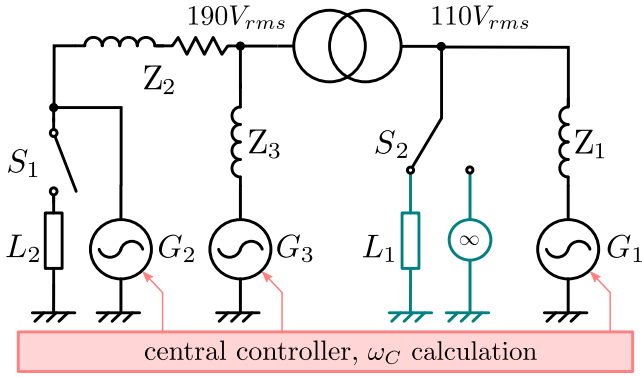


Figure 9: The microgrid contains three VSMs and a transformer. S_2 allows either connecting the microgrid to a load L_1 or to an infinite bus (grid simulator). L_2 can be disconnected by S_1 . A CC communicating with all three VSMs calculates ω_C .

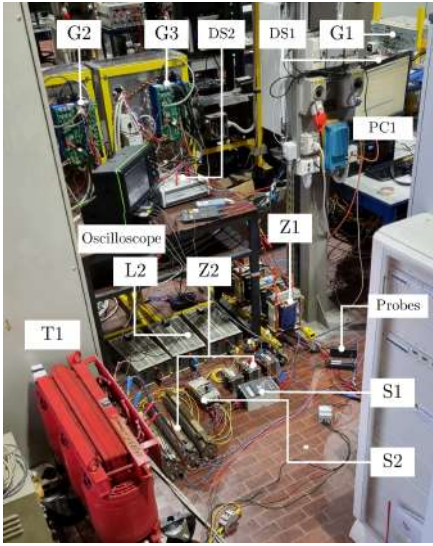


Figure 10: View of the experimental setup.

the scenario when the microgrid is connected to the infinite bus, which imposes a frequency drop (such as occurring after the loss of a generation unit in the main grid). We consider 5 different scenarios, see Tab. I: a reference case with minimum damping (LOW), a case using frequency droop (D), a case using mainly high-frequency droop (DHF) and two cases using virtual friction (VF, VFS). The grid is uniform, such that ρ is the same for each VSM.

1) Islanded grid with L_2

Fig. 11 shows experimental results with S_2 connected to L_1 (islanded grid), $J = [0.3 \ 0.1 \ 0.18] \text{kg} \cdot \text{m}^2$ and the power set points $P_{set} = [3 \ 1 \ 2] \text{kW}$, $Q_{set} = [0.7 \ 0.3 \ 0.6] \text{kVar}$. L_2 is connected at $t = 0 \text{s}$ and the subsequent change in the grounded rotor angle, frequency and output power of G_2 is observed. In scenario LOW, the grounded rotor angle δ_2 shows strong oscillations, which slowly decay over time. Scenarios D, DHF and VF exhibit similar damping performance but with small oscillations only showing for about 1s. No oscillations ensue in scenario VFS. Since the system inertia (the same in all scenarios) determines the initial rate of change of frequency (ROCOF), we see in Fig. 11b that these are identical. The VSMs have the same low frequency droop in scenarios LOW,

Scenario	D_{LF}	D_{HF}	F	ρ	σ
LOW	1	1	0	2	0
D	6	6	0	12	0
DHF	1	6	0	12	0
VF	1	1	5	12	0.83
VFS	1	1	10	22	0.91

Table I: Scenarios LOW, D, DHF, VF, VFS: the damping coefficients are chosen such that scenarios D, DHF and VF have comparable damping (same ρ). LOW and VFS have lower and higher damping respectively. ρ is defined using D_{HF} . To get the damping coefficients used for each VSM in a specific experiment, the ρ of the corresponding scenario must be multiplied by the inertia J of the corresponding VSM, which we give for each experiment.

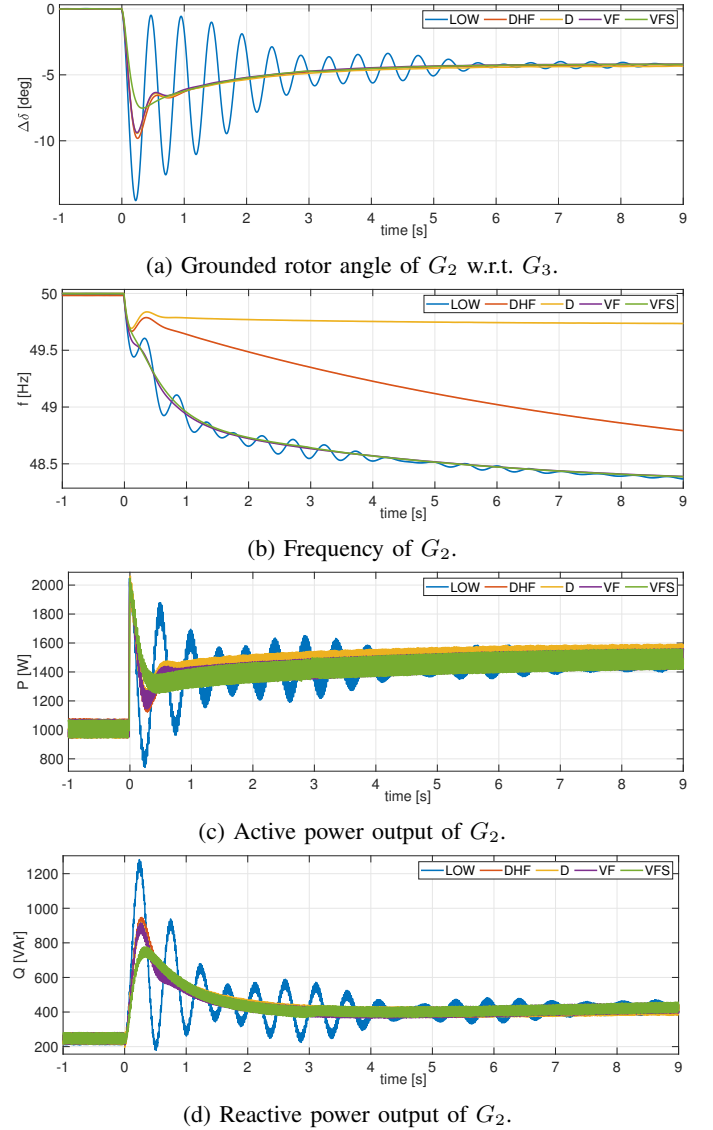


Figure 11: Load step change by connection of L_2 . VF and frequency droop perform equally well in damping the system.

DHF, VF and VFS, so that ω_2 converges to the same steady state value. Since DHF has a stronger initial action against changes of frequency, the convergence in scenario DHF is slower. Damping is the strongest in VFS, and similar damping is observed in scenarios D, DHF and VF.

In Fig. 11, the active power $P_{e,2}$ reaches a peak of 2kW in all scenarios, in part due to the inertial action of G_2 , and later converges to 1.5kW. Again, same damping is observed

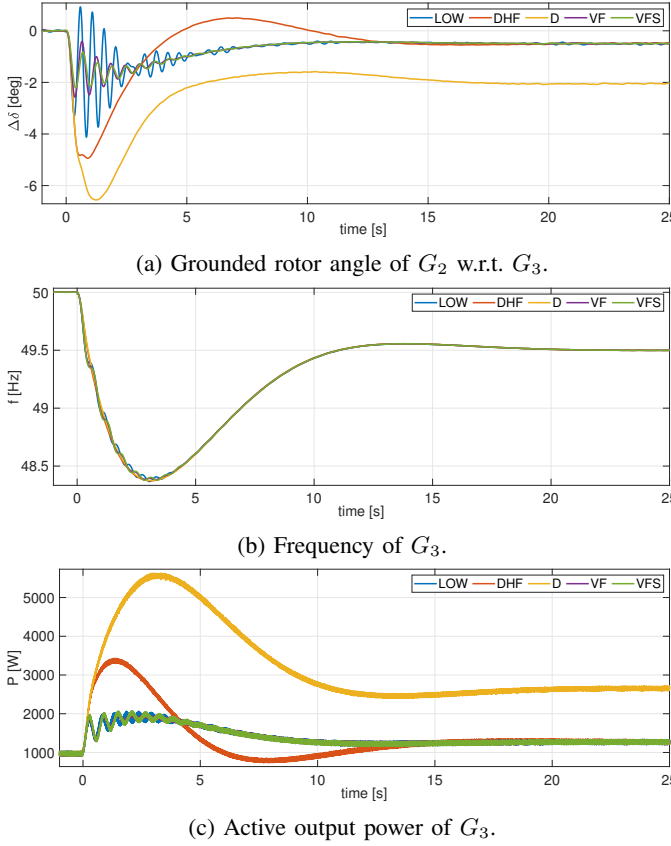


Figure 12: The effects of a frequency drop in grid connected mode: VF requires a much lower increase in output power during the event, however some oscillations remain with VF.

with D, DHF and VF, while in scenario LOW strong power oscillations appear. For completeness, we also show the reactive power output Q_2 . Similar to the active power, after an initial peak, the reactive power converges to a steady state with oscillations mainly occurring in scenario LOW. In the subsequent experiments, we do not show the reactive power output. Note that VF and frequency droop show equivalent damping performance.

2) Grid connected mode with grid frequency unknown to the CC

In Fig. 12, we show results when the microgrid is part of a larger main grid. S_1 is open, $P_{set} = [2 \ 1 \ 1]$ kW, $Q_{set} = [0.7 \ 0.3 \ 0.6]$ kVar and the inertias J_j are as in the previous subsection. Starting at $t = 0$ s, we impose a frequency drop such as usually caused by the loss of a larger generation unit in a grid. The frequency reaches a minimum of 48.4 Hz before converging to a steady state value of 49.5 Hz around $t = 30$ s. Oscillations of δ_2 , ω_2 and P_2 are strongest in scenario LOW. While the maximal excursions of δ_2 are lowest in scenarios VF and VFS, some (damped) oscillations remain. Scenarios D and DHF do not exhibit oscillations, however entail a strong increase in active output power (Fig. 12c). As expected, this power increase is minimal in scenarios VF and VFS.

The above two experiments demonstrate the effectiveness of VF in damping oscillations for islanded microgrids where all virtual rotor frequencies are known. However, if this microgrid is not islanded anymore and without additional damping acting

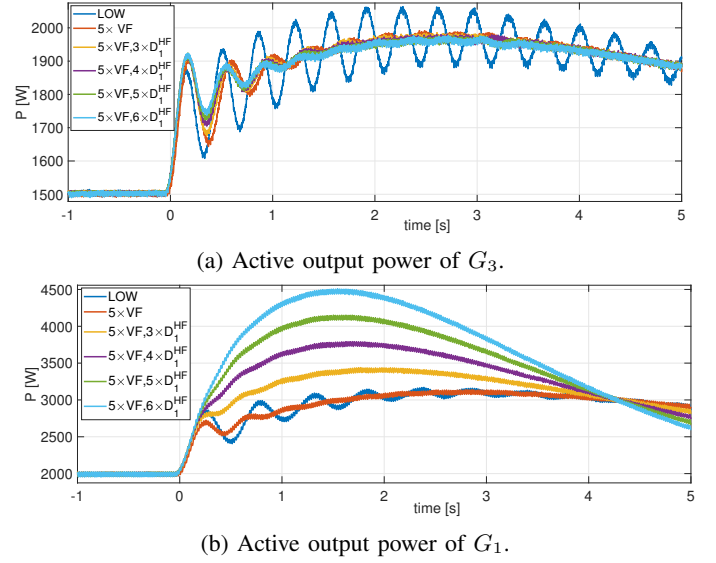


Figure 13: Active output power of G_1 and G_3 in grid connected mode after a frequency drop, for different values of HF-droop of G_3 : if only one generator can provide frequency droop, other generators can be damped effectively by using VF.

on the link between the microgrid and the main grid, VF is less effective. In such a case, it can be sufficient to increase the HF-droop on one selected VSM in order to strengthen the damping link with the main grid, while maintaining a lower droop on the remaining two VSMs. Such a configuration may be of interest if not all VSMs are connected to power sources with the capability to deliver excess power on demand. We show in Fig. 13 that such a measure can achieve good damping for even those VSMs that cannot implement high frequency droop. Fig. 13 shows the power output of VSM 3 (top) and VSM 1 (bottom) for the scenarios LOW (blue) and VF (red) as before. Using settings based on scenario VF, the other curves show the output powers when the high frequency droop of VSM 1 is increased: $D_{HF,1} = \{3, 4, 5, 6\}$. This leads VSM 1 to respond with an increasingly large power output, while VSM 3 benefits from increasingly high damping. The performance of this mechanism depends on the ratio of the inertias $\frac{J_1}{\sum J_j}$, i.e., sufficiently large inertia is required on the VSM providing high frequency droop to impact ω_C in a satisfactory manner.

Finally, Fig. 14 shows the power output of the three VSMs for scenarios LOW and VFS for the above experiment. Unlike in scenario LOW, the oscillations in VFS are strongly aligned in phase, which shows that damping between the generators is strong: they oscillate almost like a single unit against the infinite bus when VF is strong. This behavior is expected, since VF has no information about the outside grid and therefore only applies damping to inter-machine oscillations. In the next section we show a possible extension to the ω_C calculation that can solve this drawback more effectively.

3) Grid connected mode with known grid frequency

An alternative to using frequency droop on at least one of the machines to achieve damping w.r.t. the main grid is the addition of the main grid frequency in the formula for ω_C . To do so, we treat the main grid as an additional VSM with frequency ω_∞ and inertia J_∞ . This ω_∞ can be obtained for

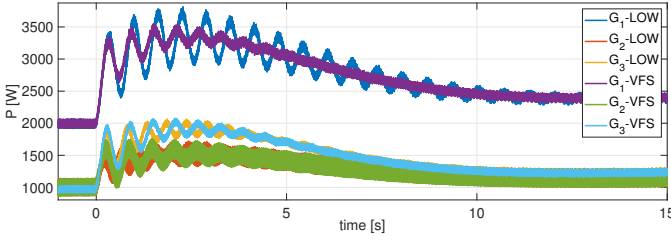
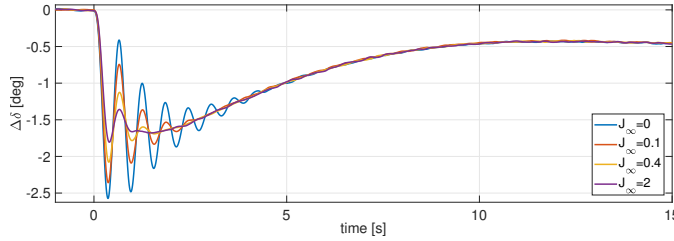
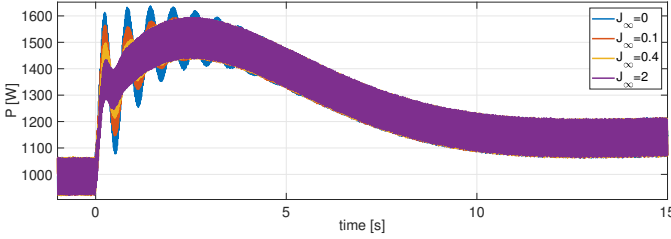


Figure 14: Oscillations in active output power of the three VSMs, comparing scenarios LOW and VFS in grid connected operation. With VF, the oscillations are synchronized.



(a) Grounded angle of G_2 w.r.t G_3 .



(b) Active power output of G_2 .

Figure 15: Oscillations in grid connected mode with different J_∞ : taking into account the infinite bus frequency ω_∞ , damping can be improved in grid connected mode.

example from a PLL placed in the main grid. The modified ω_C is defined as:

$$\omega_C = \frac{\sum_{k=1}^N J_k \omega_k + J_\infty \omega_\infty}{\sum_{k=1}^N J_k + J_\infty}. \quad (22)$$

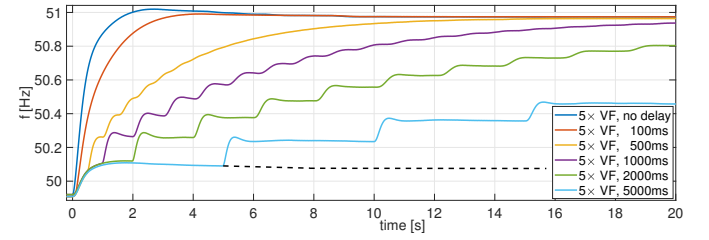
In this formula, a suitable value for J_∞ must be chosen that is comparable to the total inertia in the microgrid. Fig. 15 shows how (22) can improve the damping performance of VF with different J_∞ between $0 \text{ kg} \cdot \text{m}^2$ and $2 \text{ kg} \cdot \text{m}^2$ for the system as in Sect. IV-A2. Good damping was obtained for $J_\infty = 2 \text{ kg} \cdot \text{m}^2$, which corresponds to $\frac{J_\infty}{(J_1 + J_2 + J_3)} = 3.44$.

B. Impact of transmission delays

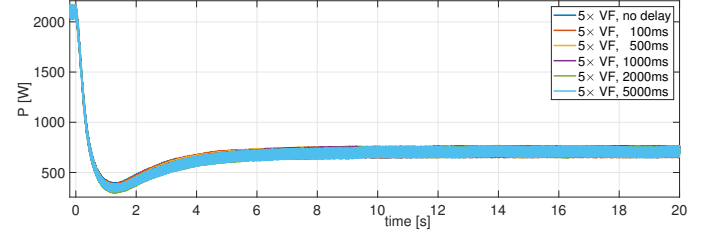
In the following, we focus on the system behavior when delays are not negligible. To clearly demonstrate the effects of delays, we first show data with the simpler, continuous delay **model 1**, discussed in Sect. III-C. We first show experiments with equal and unequal delays in an islanded microgrid, followed by cases where the generators are part of a larger grid. In Sect. IV-B5 we show results with delay **model 2**.

1) Even delays in an isolated microgrid

It was shown theoretically in Sect. III-C that in a uniform, islanded grid, equal delays (equal delays can be achieved



(a) Frequency of G_2 .



(b) Active power of G_2 .

Figure 16: Behavior of G_2 for different continuous communication delays. With increasing delay, the frequency shows a more and more slow staircase shape. No impact of the delay on the output powers of the inverters is observed.

by aligning signals at the CC and the generators) do not impact the power output. We show here an experiment with the same delay on all connection lines with round-trip delays from 0ms to 5000ms. The 3 VSMs are configured according to scenario VF with $J = [0.5 \ 0.4 \ 0.65] \text{ kg} \cdot \text{m}^2$. Initially, $P_{set} = [2 \ 2 \ 1] \text{ kW}$. At $t = 0\text{s}$, a step change in $P_{set,3} = 6 \text{ kW}$ is applied (here no low pass filter on P_{set} was used). This constitutes a large disturbance in the grid. The output power of G_2 is shown in Fig. 16a. Since the power balance in the microgrid is almost only defined by the connected loads, ω_C increases subsequent to the load step until the droop mechanism restores the power balance (Fig. 16b). It can be seen that in all cases, the system behaves stable and no impact on the power output of the generators is seen. However, ω_C shows a more and more staircase like behavior for increasing delays. A black dashed line indicates the continuation of the light blue curve before $t = 5\text{s}$. All curves in Fig. 16b follow this black dashed line until one roundtrip delay has passed since the disturbance. We recall here Sect. III-C where it was shown that equal delays cannot destabilize the system; Instead they slow down the dynamics of ω_C . An intuitive explanation is as follows: the initial frequency increase is caused by the disturbance itself, while the ω_C received by the VSMs is still the same. In this initial phase, scenario D would produce identical results with scenario VF. After sufficient time has passed, the VSMs receive the new ω_C and react again with an increase in frequency. This process repeats indefinitely.

2) unequal delays in an isolated microgrid

The previous results showed the immunity of the power output to equal delays. In this section, we focus on unequal delays. As discussed in Sect. III-D, the most disadvantageous delays are those where the roundtrip delay of one of the generators is close to time-period of the oscillations. In the following, we define a base delay τ_b for each experiment,

which is chosen such that it matches the half-period of the expected oscillations. A configuration of delays is denoted by djk , with $j, k \in \{0, 1, 2, 3, A\}$. By $j \in \{1, 2, 3\}$, we mean that the communication from G_j to the CC is delayed by τ_b , whereas 0 means that the CC receives all signals undelayed. The letter A indicates that all three data lines from the VSMs to the CC are delayed by τ_b . k refers to the data lines from the CC to the VSMs in the same way. For example, d3A means that data from G_3 to the CC is delayed by τ_b and all generators receive ω_C with a delay τ_b . However, the data-lines of G_1 and G_2 towards the CC are not delayed. In Sect. IV-B5 we will further use the letter S , to indicate that the samples are aligned in case of a random delay.

Fig. 17 shows the grounded angle, frequency and active power of G_1 subsequent to a connection of L_2 . The 3 VSMs are configured according to scenario VF with $\tau_b = 320\text{ms}$, $J = [0.4 \ 0.2 \ 0.2]\text{kg} \cdot \text{m}^2$ ($f = 0.83$, $\rho = 12$), $P_{set} = [3 \ 1 \ 2]\text{kW}$ and $Q_{set} = [600 \ 500 \ 300]\text{Var}$. In this experiment, J is such that for low damping, G_2 and G_3 oscillate against G_1 . A delay impacting the communication between G_1 and the CC thus is the most detrimental. In this plot we compare d00 (no delay), d10 (delays only from G_1 to the CC) and d11 (delays both ways between G_1 and the CC) with two compensation techniques: dA1 (alignment of all signals at the CC and thus a delay on all data lines VSM to CC) and dAA (alignment at the CC and also at the generators). The lowest damping is seen in case d11, where the roundtrip delay between G_1 and the CC matches the oscillation period. If in such a case, the signals are aligned at the CC (dA1), the damping improves significantly. The grounded angles and active power output for delay cases d00, d10, dAA are identical, as predicted by the theory in Sect. III-C: in these three cases, all three VSMs receive the same $\tilde{\omega}_C$. Fig. 17b shows that the speed of convergence of the frequency increases with the number of impacted communication lines from d00 to dAA.

3) Correlation of oscillation frequency and delay

In Sect. III-D we showed, how the damping k and the frequency ν are impacted by unequal delays. The strongest decrease in the VF-damping was observed in the simple 2-VSM system if $\tau = \tau_0$. In the experimental 3-VSM grid, a similar dependence can be observed, see Fig. 18. Here the VSMs are as in Sect. IV-B2 with delay configuration d11 (the “worst” case). After (dis)connecting L_2 , we observe the oscillations of G_1 for different delays. For each experiment with a certain delay τ_b , the damping k and oscillation frequency ν can be estimated by curve fitting (as previously described in Sect. III-D). The obtained values for k and ν are plotted as functions of τ_b in Fig. 18a. Solid lines indicate values for the experiment conducted when connecting L_2 and dashed lines when disconnecting L_2 . The black line is a plot of the frequency $f_\tau = 1/(2\tau_b)$. It can be observed that the damping is lowest when τ_b matches the oscillation half-period (the intersection between the black and the blue lines) at $\tau_b \approx 0.35$. The output power of G_1 is shown for selected τ_b in Fig. 18b. The lowest damping is seen for the yellow curve where $\tau_b = 0.350\text{s}$, which matches the peak in Fig. 18a. In this

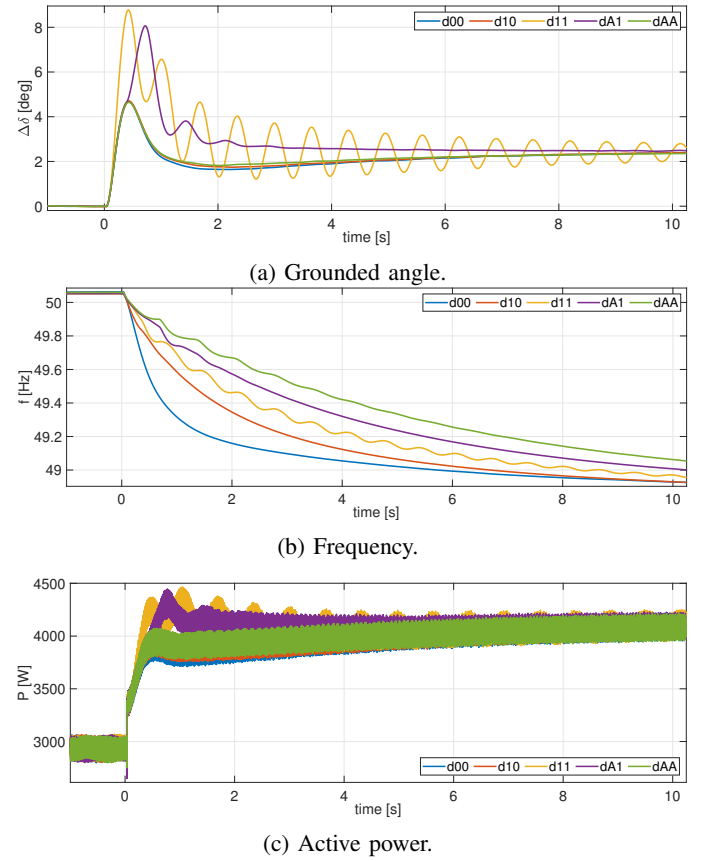


Figure 17: Behavior of G_1 subsequent to L_2 connection with unequal delays: if the VSMs receive the same signal ω_C , no impact on the output power is observed.

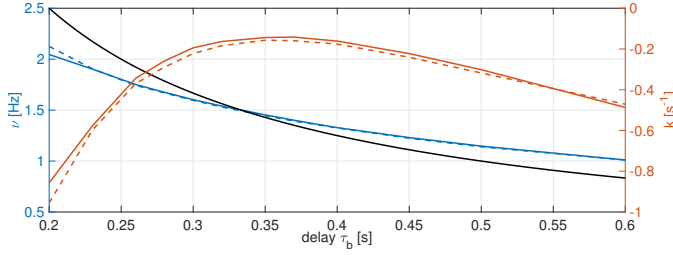
case, the oscillation period is $700\text{ms} = 2\tau_b$, as expected. These results match well with the observations made in Sect. III-D.

4) Delays in grid connected operation

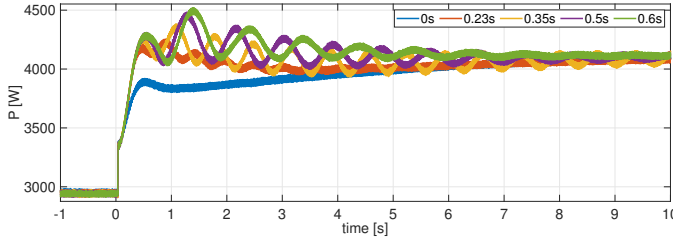
The above delay analysis was done for an isolated microgrid. While in grid connected mode (as in Sect. IV-A2) with unequal delays the same observations can be made as in an isolated grid, increasing delays in this case can change the power output of the VSMs during a frequency drop. Fig. 19 shows such an experiment where ω_∞ is as in Sect. IV-A2. The delay configuration is dA0 (where also ω_∞ is delayed by τ_b), $J_\infty = 1\text{kg} \cdot \text{m}^2$, $J = [0.2 \ 0.1 \ 0.07]\text{kg} \cdot \text{m}^2$ ($f = 0.83$, $\rho = 12$), $P_{set} = [1 \ 1.5 \ 1.2]\text{kW}$, $Q_{set} = [600 \ 200 \ 200]\text{Var}$. In such a scenario, delays lead to an increase in the output power of the VSMs: while $t < \tau_b$, the power output and the grounded angles behave like in scenario D (blue), since during this initial interval following the start of the frequency drop, the received $\tilde{\omega}_C$ remains constant. When $t \geq \tau_b$, the VSMs start receiving information about the frequency drop and the output power decreases.

5) Random delays

We show here results with the delay **model 2** in the islanded case. Damping is as in scenario VF, $J = [0.4 \ 0.2 \ 0.2]\text{kg} \cdot \text{m}^2$, $P_{set} = [3 \ 1 \ 2]\text{kW}$, $Q_{set} = [600 \ 500 \ 300]\text{Var}$. If signal alignment at the CC is performed in a scenario, we denote this by dAA. Here $\tau_{min} = \tau_{var,max} = 200\text{ms}$. This choice is made so that $\tau_{min} + \frac{1}{2}\tau_{var,max} = 300\text{ms}$, which is approximately the

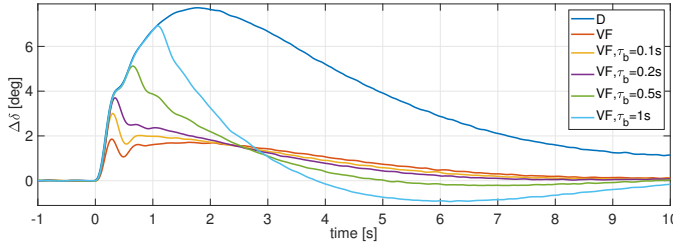


(a) Oscillation frequency ν and damping k as a function of delay τ_b for disturbances created by (dis-)connecting L_2 . The black line marks $f_\tau = 1/(2\tau_b)$. Damping k is worst for $\tau_b \approx 0.35$, which matches the oscillation-half period, i.e. $f_\tau = \nu$.

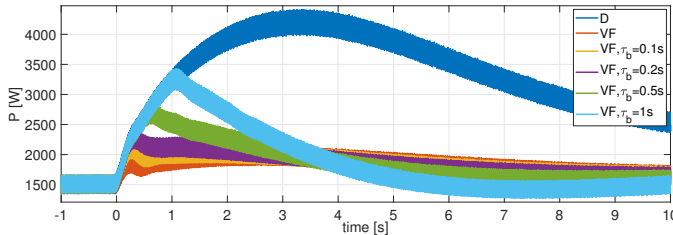


(b) Power output of G_1 for selected delays. Connection of L_2 at $t = 0$ s.

Figure 18: Oscillations with delay setting d11 for different τ_b : damping is lowest when roundtrip delay and oscillation period match.



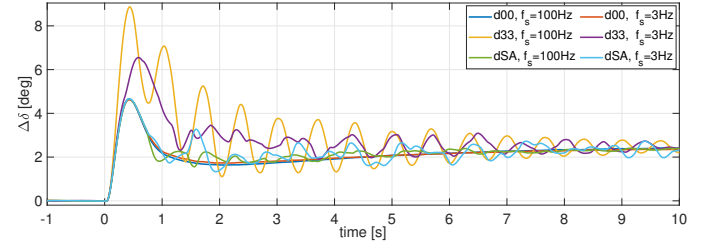
(a) Grounded angle.



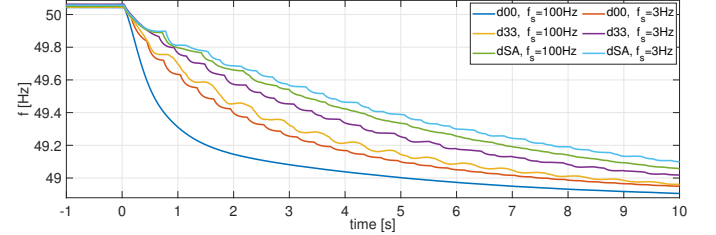
(b) Power output.

Figure 19: Behavior of G_2 for different τ_b in grid connected mode subsequent to a frequency drop: during the initial phase where ω_C is not yet representing the frequency drop, VF behaves like frequency droop.

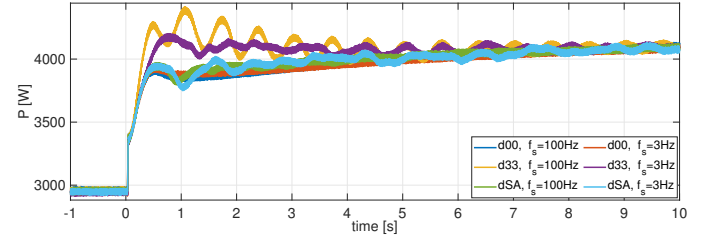
half-period of the expected oscillations and thus again close to the worst case. We compare the delay cases d00, d33 and dAA for sampling frequencies of 100Hz and 3Hz in Fig. 20. A sampling rate of 100Hz does not visibly impact the system behavior (dark blue). No impact on grounded angle and power output is seen if the sampling frequency is decreased to 3Hz. However, the system frequency converges slower, similar to what was observed in Sect. IV-B1. The case d33 with 100Hz sampling frequency shows similar results as with delay **model 1**, with weak damping. Decreasing the sampling frequency to 3Hz in this case further slows down the frequency dynamics and disturbances become less regular (however they persist



(a) Grounded angle.



(b) Frequency.



(c) Active power.

Figure 20: Impact of delays on G_1 in isolated microgrid subsequent to L_2 disconnection with delay **model 2**: the sampling frequency causes additional disturbances, however the nonlinear delays seem to prevent strong oscillations from occurring.

for an equally long time). Finally, aligning signals at the CC while delays on all three channels from the CC to the VSMs are equal leads to the slowest frequency convergence. In this case however, the peak in grounded angle and output power observed in case d33 does not occur and disturbances are less pronounced.

V. CONCLUSIONS

We provide a theoretical and experimental evaluation of VF in a microgrid when communication channels introduce delays. We show that VF allows decoupling frequency support from damping and can be used as an effective tool for microgrids where strong frequency droop cannot be used due to limitations of the primary energy sources. The theoretical analysis shows that equal delays cannot deteriorate the damping effect of VF. For delays > 100 ms the frequency convergence in isolated microgrids is slower than without delays. Unequal delays can cause ω_C to oscillate and, if the delays are close to the oscillation half-period, can deteriorate damping. Such delays can be avoided by aligning individual signals at the CC and potentially at the VSMs, using timestamps. An extension of the COI calculation is introduced that strengthens damping of VSMs against the main grid. Finally, a random delay model is tested. The presented theoretical and experimental results suggest that delays as occurring in real communication systems can be compensated by simple mechanisms such as signal alignment. Further research is suggested to investigate

the risks of cyberattacks and communication losses as well as more complex delay compensation mechanisms such as Smith predictors.

REFERENCES

- [1] F. Reissner, V. Mallemaci, F. Mandrile, R. Bojoi, and G. Weiss, "Virtual friction: Experimental validation in a microgrid of 3 virtual synchronous machines," in *2022 IEEE 23rd Workshop on Control and Modeling for Power Electronics (COMPEL)*, Tel Aviv, Israel, 2022.
- [2] Q.-C. Zhong and G. Weiss, "Static synchronous generators for distributed generation and renewable energy," in *2009 IEEE/PES Power Systems Conference and Exposition*, 2009, pp. 1–6.
- [3] J. Alipoor, Y. Miura, and T. Ise, "Distributed generation grid integration using virtual synchronous generator with adaptive virtual inertia," in *IEEE Energy Conversion Congress and Exposition*, Denver, CO, 2013, pp. 4546–4552.
- [4] Q.-C. Zhong and T. Hornik, *Control of power inverters in renewable energy and smart grid integration*. John Wiley & Sons, Chichester, UK, 2013.
- [5] S. Dong, Y. Chi, and Y. Li, "Active voltage feedback control for hybrid multiterminal hvdc system adopting improved synchronverters," *IEEE Transactions on Power Delivery*, vol. 31, no. 2, pp. 445–455, 2016.
- [6] O. Mo, S. D'Arco, and J. Suul, "Evaluation of virtual synchronous machines with dynamic or quasi-stationary machine models," *IEEE Trans. on Industrial Electronics*, vol. PP, pp. 1–1, 12 2016.
- [7] S. Dong and Y. C. Chen, "Adjusting synchronverter dynamic response speed via damping correction loop," *IEEE Transactions on Energy Conversion*, vol. 32, no. 2, pp. 608–619, 2017.
- [8] J. Roldán-Pérez, A. Rodríguez-Cabero, and M. Prodanovic, "Parallel current-controlled synchronverters for voltage and frequency regulation in weak grids," *The Journal of Engineering*, vol. 2019, no. 17, pp. 3516–3520, 2019.
- [9] M. Chen, D. Zhou, and F. Blaabjerg, "Modelling, implementation, and assessment of virtual synchronous generator in power systems," *Journal of Modern Power Systems and Clean Energy*, vol. 8, no. 3, pp. 399–411, 2020.
- [10] V. Mallemaci, F. Mandrile, S. Rubino, A. Mazza, E. Carpaneto, and R. Bojoi, "A comprehensive comparison of virtual synchronous generators with focus on virtual inertia and frequency regulation," *Electric Power Systems Research*, vol. 201, p. 107516, 2021.
- [11] D. B. Rathnayake, M. Akrami, C. Phurailatpam, S. P. Me, S. Hadavi, G. Jayasinghe, S. Zabihi, and B. Bahrani, "Grid forming inverter modeling, control, and applications," *IEEE Access*, vol. 9, pp. 114 781–114 807, 2021.
- [12] M. Blau and G. Weiss, "Synchronverters used for damping inter-area oscillations in two-area power systems," in *Int. Conf. on Renew. Energies and Power Quality (ICREPQ)*, Salamanca (Spain), 2018.
- [13] F. Reissner, H. Yin, and G. Weiss, "A stability result for network reduced power systems using virtual friction and inertia," *IEEE Transactions on Smart Grid*, vol. 13, no. 3, pp. 1668–1678, 2022.
- [14] P. Kundur, N. J. Balu, and M. G. Lauby, *Power system stability and control*. McGraw-hill New York, 1994, vol. 7.
- [15] J. Machowski, J. W. Bialek, and J. R. Bumby, *Power System Dynamics*. Hoboken, NJ: John Wiley & Sons, 2008.
- [16] F. Reissner and G. Weiss, "The region of attraction of a grid with virtual synchronous machines employing virtual friction," in *13th IEEE International Symposium on Power Electronics for Distributed Generation Systems (PEDG)*, Kiel, Germany, 2022.
- [17] B. Yang, K. V. Katsaros, W. K. Chai, and G. Pavlou, "Cost-efficient low latency communication infrastructure for synchrophasor applications in smart grids," *IEEE Systems Journal*, vol. 12, no. 1, pp. 948–958, 2016.
- [18] J. Rischke, P. Sossalla, S. Itting, F. H. P. Fitzek, and M. Reisslein, "5g campus networks: A first measurement study," *IEEE Access*, vol. 9, pp. 121 786–121 803, 2021.
- [19] J. Pilz, M. Mehlhose, T. Wirth, D. Wieruch, B. Holfeld, and T. Haustein, "A tactile internet demonstration: 1ms ultra low delay for wireless communications towards 5g," in *2016 IEEE Conference on Computer Communications Workshops (INFOCOM WKSHPS)*, 2016, pp. 862–863.
- [20] A. Nasrallah, A. S. Thyagaturu, Z. Alharbi, C. Wang, X. Shao, M. Reisslein, and H. ElBakoury, "Ultra-low latency (ull) networks: The ieee tsn and ietf detnet standards and related 5g ull research," *IEEE Communications Surveys & Tutorials*, vol. 21, no. 1, pp. 88–145, 2019.
- [21] F. Krasniqi, A. Maraj, and E. Blaka, "Performance analysis of mobile 4g/5g networks," in *2018 South-Eastern European Design Automation, Computer Engineering, Computer Networks and Society Media Conference (SEEDA_CECNSM)*, 2018, pp. 1–5.
- [22] J. Jay, "Low signal latency in optical fiber networks," in *Proc. of the 60th IWCS*, Conference, Charlotte, NC, USA, 2011.
- [23] D. Del Rivero, P. G. Fernández, C. Blanco, and Á. Navarro-Rodríguez, "Control of aggregated virtual synchronous generators including communication delay compensation," in *2022 IEEE Energy Conversion Congress and Exposition (ECCE)*. IEEE, 2022, pp. 1–7.
- [24] Y. Khayat, Q. Shafiee, R. Heydari, M. Naderi, T. Dragičević, J. W. Simpson-Porco, F. Dörfler, M. Fathi, F. Blaabjerg, J. M. Guerrero, and H. Bevrani, "On the secondary control architectures of ac microgrids: An overview," *IEEE Transactions on Power Electronics*, vol. 35, no. 6, pp. 6482–6500, 2020.
- [25] Z. Wang, Y. Chen, X. Li, Y. Xu, C. Luo, Q. Li, and Y. He, "Active power oscillation suppression based on decentralized transient damping control for parallel virtual synchronous generators," *IEEE Transactions on Smart Grid*, 2022.
- [26] Z. Kustanovich, S. Shrivatri, H. Yin, F. Reissner, and G. Weiss, "Synchronverters with fast current loops," *IEEE Transactions on Industrial Electronics*, in press, early access.
- [27] V. Natarajan and G. Weiss, "Synchronverters with better stability due to virtual inductors, virtual capacitors, and anti-windup," *IEEE Trans. on Industrial Electronics*, vol. 64, no. 7, pp. 5994–6004, 2017.
- [28] Z. Kustanovich, F. Reissner, S. Shrivatri, and G. Weiss, "The sensitivity of grid-connected synchronverters with respect to measurement errors," *IEEE Access*, vol. 9, pp. 118 985–118 995, 2021.
- [29] P. Lorenzetti and G. Weiss, "Saturating PI control of stable nonlinear systems using singular perturbations," *IEEE Transactions on Automatic Control*, 2022, early access.
- [30] F. Dörfler and F. Bullo, "Synchronization and transient stability in power networks and nonuniform Kuramoto oscillators," *SIAM J. on Control and Optimization*, vol. 50, no. 3, pp. 1616–1642, 2012.
- [31] G. Weiss, F. Dörfler, and Y. Levron, "A stability theorem for networks containing synchronous generators," *Systems & Control Letters*, vol. 134, p. 104561, 2019.
- [32] H.-D. Chiang, *Direct Methods for Stability Analysis of Electric Power Systems: Theoretical Foundation, BCU Methodologies, and Applications*. Hoboken, NJ: John Wiley & Sons, 2011.
- [33] P. Sauer and M. Pai, *Power System Dynamics and Stability*. Stipes Publishing LLC, Champaign, Illinois, 1997.
- [34] G. Weiss, Q.-C. Zhong, T. Green, and J. Liang, " H^∞ repetitive control of DC-AC converters in microgrids," *IEEE Transactions on Power Electronics*, vol. 19, no. 1, pp. 219–230, 2004.
- [35] Á. Navarro-Rodríguez, C. Blanco, P. García, and M. I. Yousuf, "Improved delay compensation in communication-based hierarchical control of a low voltage 3-phase ac microgrid using a secondary control based on smith predictor," in *2021 IEEE Energy Conversion Congress and Exposition (ECCE)*, 2021, pp. 1116–1121.
- [36] W. Lewandowski and C. Thomas, "GPS time transfer," *Proceedings of the IEEE*, vol. 79, no. 7, pp. 991–1000, 1991.